star-forming regions. Fig. 4(d) shows that the extended emission is more pronounced at 1.5 GHz than at 6.3 GHz in similar areas of the galaxy (as the colours are identical according to the spectral index, see Table 7 for a more quantitative comparison). This can be explained by the fact that, at higher frequencies, the synchrotron emission traces younger and more energetic CRes, which are still close to their birthplace in star-forming regions. At lower frequencies, we observe the synchrotron radiation of the older CRes, which are already diffused away to longer distances and to larger scales along the ISM's magnetic field.

As shown by Corbelli, Braine & Tabatabaei (2020), the 5 GHz TH radio sources in M 33 represent the early phases of star formation, such as YSOs and H II regions. Many of these sources with no associated SNRs emit NTH emission. They also indicate the role of massive stars in the enhancement of the magnetic field and in the acceleration of CRes.

Table 7 quantifies the contribution of each structural component in the TH and NTH emission. As mentioned, the 1.5 GHz NTH emission emerges mainly from the diffuse disc (∼44 per cent) and from extended structures (∼26 per cent). At the higher frequency 6.3 GHz, the contribution of diffuse emission drops, instead the NTH emission from discrete sources increases (∼40 per cent). The TH emission is dominated by the emission from the sources at both frequencies (∼55 per cent). Hence, about 45 per cent of the TH free–free emission must emerge from the diffuse ionized gas (DIG) with spatial scales of >200 pc. This agrees with the contribution of the DIG in the total Hα emission observed in galaxies (e.g. Ferguson et al. 1998; Greenawalt et al. 1998)

In the inner 18 × 18 arcmin^2 disc of M 33, about 40 per cent of the total observed flux density at 6.3 GHz is due to TH free–free emission, while it is 25 per cent at 1.5 GHz. The origin of the observed structures differs in terms of the TH and NTH radiation mechanisms as follows:

(i) The observed diffuse disc emission, which also includes possible halo emission projected on to the disc of M 33, has mainly a NTH origin (∼80 per cent at 1.5 GHz and 66 per cent at 6.3 GHz), indicating a more dominant diffusion/escape of CRes from their birthplaces in star-forming regions than ionizing UV photons.

(ii) The observed extended structures have a similar TH/NTH mixture as the diffuse disc. The extended emission follows a spiral pattern filling in the area from which no considerable TH emission emerges (Fig. 4), and it is dominated by the NTH emission.

(iii) The TH fraction of the sources is about 40 per cent (50 per cent) at 1.5 GHz (6.3 GHz). This is higher than that of the diffuse, extended components by a factor of 2 at 1.5 GHz and is about 30 per cent of that found at 6.3 GHz. The fact that more than half of the radio sources are H II regions with a flat spectrum (Section 4.1.1) can explain this difference.

The synchrotron emission of the CRes thus shapes the diffuse and extended components of the RC emission in M 33. This provides further hints on the distribution of the magnetic fields in the ISM traced by the synchrotron emission. The spiral pattern of the large-scale field can explain the observed extended structure of the NTH emission at 1.5 GHz. This agrees with the earlier polarization studies at ∼0.5 kpc linear resolutions (Tabatabaei et al. 2007b, 2008). The smooth NTH disc component can be linked to an isotropic random magnetic field component in the disc.

Compared to that at 1.5 GHz, a newer generation of cosmic rays, which still have not diffused that far from star-forming regions, produces the synchrotron emission at 6.3 GHz. Hence, the magnetic

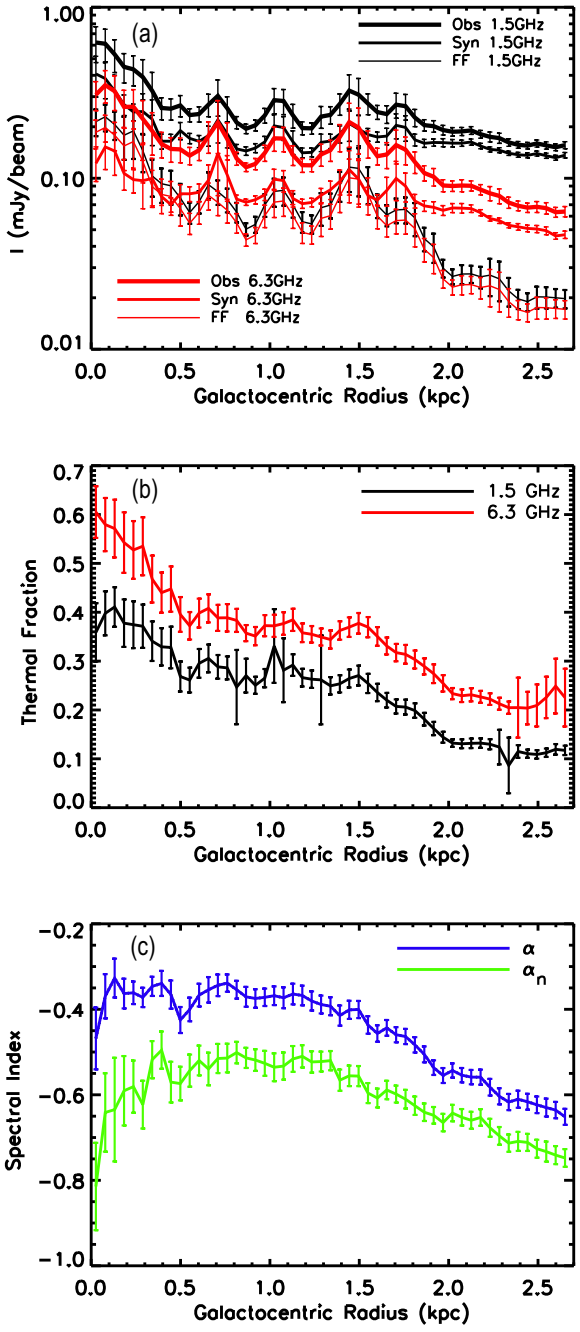

Figure 5. The radial profiles of the RC emission at 1.5 and 6.3 GHz and their NTH synchrotron and TH free–free components (a). Also shown are the radial profiles of the TH fraction (b) and the spectral index (c) for the observed RC emission (α) and its NTH component (α_n). Background radio sources are subtracted.

field structures in star-forming regions should be better traced by this emission at 6.3 GHz.

The radial profile of the RC emission obtained by averaging the intensities in rings of 15 arcsec width centred at RA = $01^h33^m50\overset{s}{.}89$ and Dec. = $+30°39'36''.8$ in the plane of M 33 (i = 56° and PA = 23°) is shown in Fig. 5(a). It is interesting to note that the inner most ring shows a peak at 1.5 GHz but not at 6.3 GHz. The peak of the 6.3 GHz radial profile occurs at the second ring i.e. about 80–90 pc from the centre. Separating the TH and NTH components, we infer that the 6.3 GHz peak is actually due to the TH emission from the young

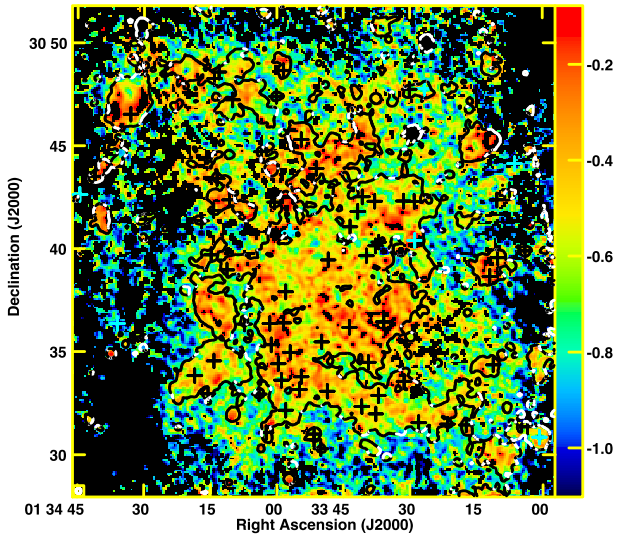

Figure 6. Map of the NTH spectral index $\alpha_{\rm n}$ ($I_\nu^{\rm nt} \sim \nu^{\alpha_{\rm n}}$) obtained between 1.5 and 6.3 GHz at 15 arcsec angular resolution overlaid with the 6.3 GHz emission contours at the level of 90 μJy beam^{-1} (8σ). Crosses show positions of the optically confirmed SNRs from Gordon et al. (1999). Background radio sources are subtracted.

star clusters surrounding the centre and that a NTH source with a relatively steep spectrum (see Section 4.3) must cause the peak of the 1.5 GHz emission at the centre. Errors are given by the rms of the pixels in the rings divided by the square root of the number of pixels per beam area.

The TH fraction varies strongly from place to place in the galaxy. This is also evident from the radially averaged values in Fig. 5(b). We note that the global decrease of the TH fraction with R is mainly due to the diffuse disc component, which is about 19 per cent at 1.5 GHz and 35 per cent at 6.3 GHz at the centre, hence just slightly higher than the total mean value. In star-forming regions, measurements result in TH fractions larger than 60 per cent (40 per cent) at 6.3 GHz (1.5 GHz).

4.3 Radio continuum spectral index

The VLA observations corrected for the short spacing and TH contamination are used to map the spectral index of the pure NTH component, $\alpha_{\rm n}$ ($I_\nu^{\rm nt} \sim \nu^{\alpha_{\rm n}}$). This allows one to investigate the interaction of CRes with the ISM even in diffuse regions. We measured both α ($I_\nu^{\rm obs} \sim \nu^{\alpha}$) and $\alpha_{\rm n}$ between 1.5 and 6.3 GHz for pixels with intensities above 2.5σ rms noise level at each frequency. The resulting map of $\alpha_{\rm n}$ obtained in the inner 18 × 18 arcmin^2 of M 33 at 15 arcsec resolution is shown in Fig. 6. The mean spectral index of the total RC is $\alpha = -0.59 \pm 0.28$, with the error the standard deviation. This is flatter than the value found for the entire galaxy M 33 ($\alpha = -0.71 \pm 0.23$), but agrees with that measured in the same area by Tabatabaei et al. (2007b).[7] The mean spectral index of the NTH emission is $\alpha_{\rm n} = -0.67 \pm 0.23$, which is slightly steeper than α. The actual uncertainty in the spectral index varies from 0.01 in the bright star-forming regions to 0.06 in fainter diffuse regions between the arms.

[7]Note that a different definition for the spectral index and a also a different distance to M 33 were used in that work.

Both the total and the NTH spectra are flatter in star-forming complexes and generally in the spiral arms than in other parts of the disc. The steeper spectra of the extended and diffuse structures can be linked to the CRes cooling when propagating away from their birthplace in star-forming regions due to interaction with the magnetized ISM. Similar to the per-source measurements (Section 4.1.1), the mapping approach leads to a typical value of $\alpha_{\rm n} \simeq -0.6$ for the SNRs.

Fig. 5(c) shows the radial variation of the spectral index. To generate these profiles, the mean ring spectral indices are determined from the distribution histograms of pixels in the 15 arcsec-wide rings, with error bars showing the statistical errors. At the centre, $\alpha_{\rm n} = -0.70 \pm 0.04$. The spectrum becomes flatter moving away from the centre out to $R \sim 1$ kpc. This is because the number of H II complexes with flat spectra increases in this radial range. At larger radii, the spectrum steepens more or less with radius out to $R \sim 3$ kpc, which is a diffuse region between the spiral arms, where it reaches its steepest ring average value of $\alpha_{\rm n} = -0.75 \pm 0.06$.

In the inner 18 × 18 arcmin^2 region of M 33, $\alpha_{\rm n}$ is generally flatter than expected for pure synchrotron cooling of CRes (i.e. $\alpha_{\rm n} \simeq -1$ which prevails in the outer parts of this galaxy, Tabatabaei et al. 2007c). This can be explained if (1) CRes re-accelerate and gain energy due to shocks in star-forming regions and (2) they do not fully loose their energy to synchrotron loss because of advection, winds, and outflows. We further discuss these processes in Section 5.

4.4 Magnetic field strength

The strength of the total magnetic field $\rm B_{tot}$ can be derived from the total synchrotron intensity. Assuming equipartition between the energy densities of the magnetic field and cosmic rays ($\varepsilon_{CR} = \varepsilon_{\rm B_{tot}} = \rm B_{tot}^2/8\pi$):

$$\rm B_{tot} = \mathit{C}(\alpha_{\rm n}, \mathit{K}, \mathit{L})\left[\mathit{I}_{\rm nt}\right]^{\frac{1}{\alpha_{\rm n}+3}}, \quad (6)$$

where $I_{\rm nt}$ is the NTH intensity and C is a function of $\alpha_{\rm n}$, K the ratio between the number densities of cosmic ray protons and electrons, and L the path length through the synchrotron-emitting medium (see Beck & Krause 2005; Tabatabaei et al. 2008). Using the obtained maps of $I_{\rm nt}$ and $\alpha_{\rm n}$ and assuming that the magnetic field is parallel to the plane of the galaxy (inclination of $i = 56°$ and position angle of the major axis of PA = 23°), $\rm B_{tot}$ is derived across the galaxy. In our calculations, we apply values of $K \simeq 100$ (Beck & Krause 2005) and $L \simeq 1\,{\rm kpc}/\cos i$.

The resulting magnetic field strength varies between 3 and 24 μG in the inner 18 × 18 arcmin^2 region of M 33 (Fig. 7). The magnetic field is stronger in star-forming complexes in the main spiral arms and in the centre than in other parts. The strongest magnetic fields are found in giant H II regions such as NGC 604 and NGC 595 with $\rm B_{tot} \geq 20\,\mu G$. A possible impact of massive star formation on the magnetic field strength is discussed in Section 5.3. The mean field strength of $\rm B = 7 \pm 1\,\mu G$ agrees with that obtained by Tabatabaei et al. (2008) in the same region, however, based on the present data, we resolve much larger variations and dynamical range of the equipartition magnetic field strength.

5 DISCUSSION

In Section 4, we studied the origin of the RC emission in terms of both physical processes (TH/NTH) and structural components (sources/extended/disc). The structural decomposition helps in calibrating empirical recipes to derive the SFR surface density using

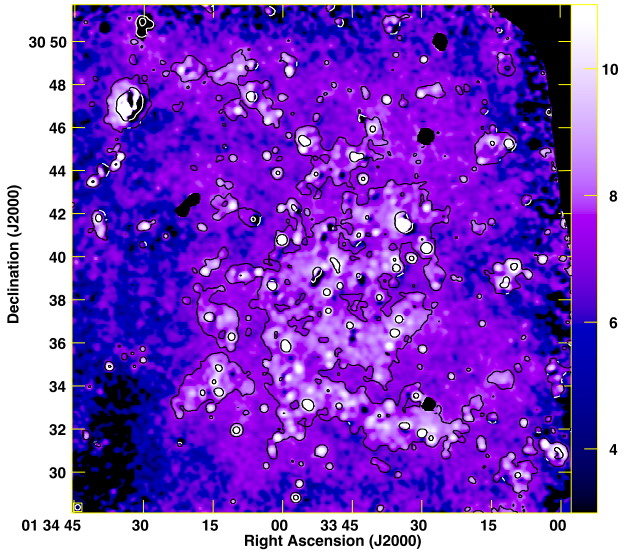

Figure 7. Map of the magnetic field strength overlaid with the 6.3 GHz emission contours at the level of 100 and 500 μJy beam^{-1}. The angular resolution of 15 arcsec is shown in the bottom-left corner of the image. Background radio sources are subtracted. The colour bar on the right-hand side indicates the magnetic B-field strength in μG.

the observed RC maps. In this section, we further exploit the results of the TH/NTH decomposition to study the impact of massive star formation on the two ISM components: the cosmic rays and magnetic field. Differentiating different physical processes and structures, the connection of the RC emitting ISM with its neutral gas phases is also investigated.

5.1 Calibrating star formation rate surface density from radio continuum

Star-forming regions are bright components of M 33 in both the TH and the NTH maps. This is expected as these regions are the most powerful sources of the RC emission produced during different phases of massive star formation. Hence, the observed RC emission itself can be used as a dust-unobscured tracer of the SFR. However, the use of the RC maps can be complicated by the diffusion of CRes and/or the generation of secondary CRes not directly linked to star formation. These effects become less pronounced by taking the RC emission from only star-forming regions in resolved studies. We address these effects and the impact of diffuse/extended emission on calibrating the SFR surface density, $\Sigma_{\rm SFR}$, by studying the SFR–RC relation separately for star-forming regions alone (sources in Fig. 4) and when including diffuse and extended emission in M 33, using the results of the structural decomposition.

The de-reddened Hα map used as a general free–free emission template in previous sections can serve as a reference SFR tracer only after removing the emission from DIG as the ionization source of the DIG can be a different one than young massive stars. However, as discussed above, diffuse regions are also considered here to investigate their effect on the calibration. To convert the de-reddened Hα luminosity density $\Sigma_{\rm H\alpha}$ to $\Sigma_{\rm SFR}$, we use

$$\left(\frac{\Sigma_{\rm SFR}}{M_\odot\,{\rm yr^{-1}kpc^{-2}}}\right) = 5.37\times10^{-42}\left(\frac{\Sigma_{\rm H\alpha_{corr}}}{\rm erg\,s^{-1}kpc^{-2}}\right). \quad (7)$$

The calibration factor is the same as that of the integrated luminosity relation given by Murphy et al. (2011). This relation measures the current ($\lesssim$10 Myr) formation rate of stars assuming a Kroupa IMF (Kroupa 2001).

The $\Sigma_{\rm SFR}$ and the RC luminosity surface densities, $\Sigma_{1.5\,\rm GHz}$and $\Sigma_{6.3\,\rm GHz}$, are first calculated for pixels with sizes of 15 arcsec. The calibration relations are then derived taking into account a 1.5σ cut off. Focusing on only star-forming regions, both the diffuse disc and the extended emission are subtracted from the radio maps.[8] A tight correlation holds between $\Sigma_{\rm SFR}$ and both $\Sigma_{1.5\,\rm GHz}$ and $\Sigma_{6.3\,\rm GHz}$ ($r\simeq0.90$, see Fig. 8) in the star-forming regions. Fitting a relation of the form $\log\Sigma_{\rm SFR}=b\ \log{\rm X}+a$, a linear relation is found between $\Sigma_{\rm SFR}$ and $\Sigma_{1.5\,\rm GHz}$, using an ordinary least square (OLS) regression (see Table 8). The correlations become steeper, particularly at 1.5 GHz, if the extended structures are also included in this process. If neither the extended emission nor the diffuse disc is subtracted, the slopes of the $\Sigma_{\rm SFR}$ relations increase by $\simeq$60 per cent and 30 per cent versus $\Sigma_{1.5\,\rm GHz}$ and $\Sigma_{6.3\,\rm GHz}$, respectively.[9] In this case, the super-linearity of the $\Sigma_{\rm SFR}$–$\Sigma_{1.5\,\rm GHz}$ correlation is similar to that obtained by Heesen et al. (2014) for the SINGS galaxies (their reported average slope of 0.63 of the RC versus $\Sigma_{\rm SFR}$ is equivalent to a slope of $\simeq$ 1.6 for the $\Sigma_{\rm SFR}$ versus $\Sigma_{1.5\,\rm GHz}$ relation). This shows the impact of diffuse emission in resolved studies of the SFR–RC correlation. The inclusion of a galaxy's diffuse regions poses a larger weight to the low-SFR regions, where the RC luminosity is enhanced due to diffused CRes or generated in secondary processes. Because these CRes have lower energies, this effect is more pronounced at lower radio frequencies ($\nu_{\rm c}\sim E^2$). This explains the different SFR–RC slopes at 1.5 and 6.3 GHz if the extended/diffuse emission is not subtracted.

Focusing only on the star-forming regions, we find the following calibration relation at 1.5 GHz,

$$\left(\frac{\Sigma_{\rm SFR_{1.5}}}{M_\odot\,{\rm yr^{-1}kpc^{-2}}}\right) = (2.81\pm0.98)\times10^{-38} \times\left(\frac{\nu\Sigma_{1.5\,\rm GHz}}{\rm erg\,s^{-1}kpc^{-2}}\right)^{(1.015\pm0.042)}, \quad (8)$$

and at 6.3 GHz,

$$\left(\frac{\Sigma_{\rm SFR_{6.3}}}{M_\odot\,{\rm yr^{-1}kpc^{-2}}}\right) = (3.55\pm0.76)\times10^{-41} \times\left(\frac{\nu\Sigma_{6.3\,\rm GHz}}{\rm erg\,s^{-1}kpc^{-2}}\right)^{(1.085\pm0.035)}, \quad (9)$$

The $\Sigma_{\rm SFR}$–$\Sigma_{6.3\,\rm GHz}$ relation is slightly steeper than the $\Sigma_{\rm SFR}$–$\Sigma_{1.5\,\rm GHz}$ one, though they overlap considering the errors. The empirical calibration relations given in equations (8) and (9) are shown as solid lines in Fig. 8. Assuming a linear proportionality between supernova rate and the SFR and using an empirical Galactic relation between the NTH spectral luminosity and the supernova rate, Murphy et al. (2011; hereafter Murphy11) presented a model calibration that depends on the NTH spectral index (their equation 15). We also obtain $\Sigma_{\rm SFR_\nu}$ using Murphy's calibration (dashed lines in Fig. 8) by adopting M 33's average $\alpha_{\rm n}=-0.67$ in the inner disc (see Section 4.3). This calibration, however, underestimates M 33's SFR by a factor of $\simeq$2 and 1.5 derived from our 1.5 and 6.3 GHz data, respectively. As explained by Murphy11, such underestimates are linked to the diffusion or escape of CRes neglected in the model. We note, however, that the deviation is within 1σ scatter of the fitted empirical relation.

[8]Background sources are subtracted as well.
[9]This steepening is even higher using the bisector regression.

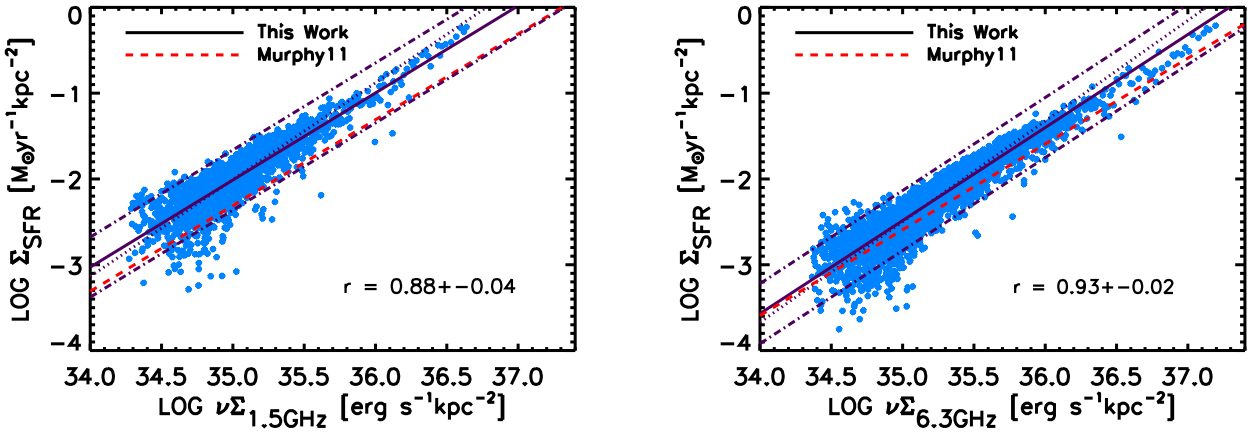

Figure 8. SFR surface density $\Sigma_{\rm SFR}$ as a function of the observed RC emission at 1.5 GHz (left) and 6.3 GHz (right) for star-forming regions in the inner disc of M 33. Lines show the OLS (solid) and bisector (dotted) fits and one σ scatter around the OLS fit (dot–dashed). Also shown is the model calibration relation (red dashed line) from Murphy et al. (2011). The Pearson correlation coefficient r is also indicated.

Table 8. SFR calibrations using the RC emission in the inner 18 × 18 arcmin^2 disc of M 33. The linear fits in logarithm scales ($\log \Sigma_{\rm SFR} = b\ \log {\rm X} + a$) obtained using the OLS (1) and bisector (2) regressions for star-forming regions (SF) only, SF and extended structure, and the entire inner disc. Correlations refer to apertures of 15 arcsec.

	X	$b^{(1)}$	$a^{(1)}$	$b^{(2)}$	$a^{(2)}$	r
SF						
	$\Sigma_{1.5{\rm GHz}}$	1.01 ± 0.04	-37.55 ± 0.35	1.13 ± 0.05	-41.52 ± 0.07	0.88 ± 0.04
	$\Sigma_{6.3{\rm GHz}}$	1.08 ± 0.03	-40.45 ± 0.21	1.17 ± 0.06	-43.56 ± 0.03	0.93 ± 0.02
SF and extended						
	$\Sigma_{1.5{\rm GHz}}$	1.23 ± 0.03	-45.08 ± 0.23	1.54 ± 0.04	-55.99 ± 0.04	0.75 ± 0.01
	$\Sigma_{6.3{\rm GHz}}$	1.11 ± 0.02	-41.23 ± 0.13	1.22 ± 0.02	-45.10 ± 0.02	0.88 ± 0.01
Entire inner disc						
	$\Sigma_{1.5{\rm GHz}}$	1.60 ± 0.02	-58.48 ± 0.23	2.02 ± 0.02	-73.10 ± 0.04	0.76 ± 0.01
	$\Sigma_{6.3{\rm GHz}}$	1.41 ± 0.02	-52.02 ± 0.13	1.58 ± 0.02	-57.98 ± 0.02	0.89 ± 0.01

5.2 Comparison with molecular gas

Studying the correlation between the RC emitting processes and the neutral gas is the first step towards understanding the pressure balance in the multiphase ISM. The TH RC component, which traces the ionized gas and can be used as a reference SFR tracer (e.g. Murphy11), is expected to correlate with neutral gas emission according to the Kennicutt–Schmidt (KS) star formation law (Kennicutt 1998). The NTH RC component, which traces the relativistic and magnetized ISM, is also stronger in star-forming regions and hence is expected to correlate with the neutral gas as well. However, it is unclear whether the correlations for the NTH component are limited to star-forming regions only, particularly as there is observational evidence showing a tight RC–molecular gas correlation, which cannot be linked to massive star formation (Schinnerer et al. 2013; Tabatabaei et al. 2018). This motivates us to investigate these correlations in M 33, separately in star-forming regions and in other parts of the ISM.

Fig. 9 shows that the RC emission agrees generally with the molecular gas traced by CO(2-1) line emission in most star-forming complexes. Apart from this agreement, it is interesting to note that the correlation drops at the locations of SNRs: The CO emission drops to below a 3σ level in most cases, particularly, for those SNRs indicated by crosses. Hence, a feedback from the SNRs is likely responsible for clearing the molecular gas in their surroundings.

The CO emission is not only weak in the presence of the SNRs. For instance, no CO emission is found in IC131, another giant H II region, hosting no SNR. This source is, however, known to be a strong X-ray emitter (Tüllmann et al. 2009).

Quantifying the correlation in the inner disc of M 33, the RC and CO maps are cross-correlated after removing the radio BG sources and convolving to the same angular resolution. Table 9 lists the correlation coefficients and the RC versus CO power-law slopes obtained through bisector fits.[10] Errors in the Pearson correlation coefficients are given by $\Delta r_c = \sqrt{1 - r_c^2}/\sqrt{n-2}$, with n being the number of pixels in an image.

In the star-forming regions, we find a modest RC–CO correlation with a Pearson coefficient of $r^{\rm SF} \simeq 0.60$, which is similar at both frequencies (slightly tighter with the NTH RC, Fig. 10) at the pixel resolution of 15 arcsec.

The observed RC emission changes with the CO emission through a sublinear relation with an exponent of $b^{\rm SF} = 0.67 \pm 0.02$. A similar relation holds between the NTH RC and CO. However, the TH–CO correlation is almost linear and agrees with the molecular K-S relation in the SINGS sample of galaxies (Bigiel et al. 2008). This correlation deviates from linearity ($b \simeq 1.25$) when also including other regions

[10]Since the correlated variables do not directly depend on each other, we fitted a power law to the bisector in each case (Isobe et al. 1990; Hoernes, Berkhuijsen & Xu 1998).

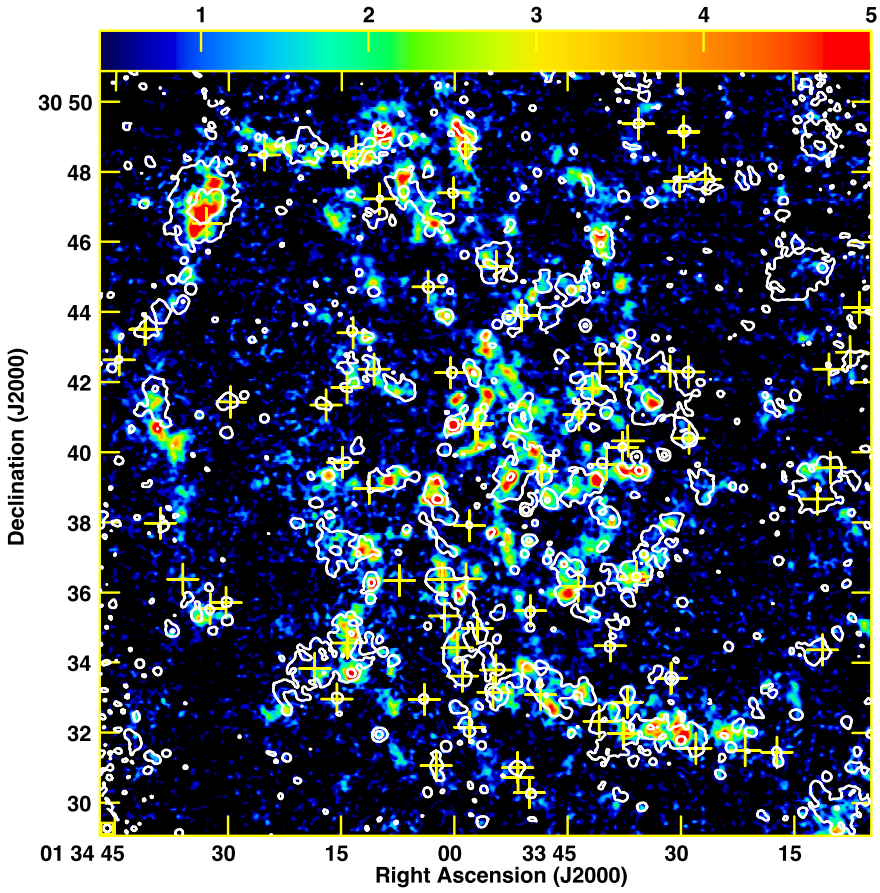

Figure 9. The CO(2-1) line emission in K km s^{-1} with contours of the radio 6.3 GHz emission overlaid. Contour levels are 50 and 750 μJy per 9 arcsec angular resolution. Circle in the lower left corner shows the 12 arcsec resolution of the CO(2-1) map. Crosses show positions of the optically confirmed SNRs from Gordon et al. (1999). Many galactic SNRs are associated with giant star-forming regions.

Table 9. Correlation between the molecular gas and observed (OBS), NTH, and TH RC emission in star-forming regions ($r^{\rm SF}$), remaining parts of the ISM ($r^{\rm extended}$), and the entire ISM (r) in the inner 18 × 18 arcmin^2 region of M 33. The corresponding power-law exponent b in the RC $\propto$ $I_{CO}{}^{b}$ relation fitted is obtained using the bisector regression. Correlations refer to apertures of 15 arcsec.

RC	$r^{\rm SF}$	$b^{\rm SF}$	$r^{\rm extended}$	$b^{\rm extended}$	r	b
1.5 GHz						
OBS	0.63 ± 0.02	0.67 ± 0.02	0.45 ± 0.01	0.29 ± 0.02	0.61 ± 0.01	0.41 ± 0.02
NTH	0.63 ± 0.02	0.65 ± 0.04	0.40 ± 0.01	0.29 ± 0.02	0.60 ± 0.01	0.50 ± 0.02
TH	0.59 ± 0.02	0.96 ± 0.04	0.31 ± 0.01	.....	0.59 ± 0.01	1.25 ± 0.04
6.3 GHz						
OBS	0.62 ± 0.01	0.68 ± 0.02	0.49 ± 0.01	0.35 ± 0.02	0.62 ± 0.01	0.79 ± 0.02
NTH	0.62 ± 0.01	0.62 ± 0.02	0.46 ± 0.01	0.33 ± 0.02	0.62 ± 0.01	0.65 ± 0.02
TH	0.57 ± 0.01	0.90 ± 0.05	0.33 ± 0.01	.....	0.59 ± 0.01	1.24 ± 0.04

of the ISM in the inner 18 × 18 arcmin^2 disc, while the quality of the correlation remains unchanged. A super-linear correlation in M 33 was already reported by Heyer et al. (2004), Verley et al. (2010), and Williams, Gear & Smith (2018), showing the mixing effect of diffuse and SF-related emission and the importance of performing structural decomposition in resolved studies.

In regions where the RC emission has an extended/diffuse structure (indicated as 'extended' in Table 9), no significant correlation holds between the TH RC and the molecular gas $r^{\rm extended} \simeq 0.30$, while the observed and NTH RC emission are still correlated with it, $r^{\rm extended} \simeq 0.45$. Hence, the RC–CO correlation is not solely due to massive star formation, as it can also hold in more quiescent regions of the ISM that is less efficient in forming those massive stars. A fine balance between the magnetic fields, CRes, and molecular gas must then hold in these regions (see e.g. Niklas 1997; Murgia et al. 2005; Tabatabaei et al. 2013a), irrespective of the origin of the magnetic field. More detailed studies are needed to dissect the origin of the magnetic fields that are important in the observed NTH RC–CO correlation. While in star-forming regions, a correlation between turbulence and magnetic fields amplified by a small-scale dynamo can play an important role in preserving the RC–CO correlation, this process is likely not as efficient in more quiescent ISM (see

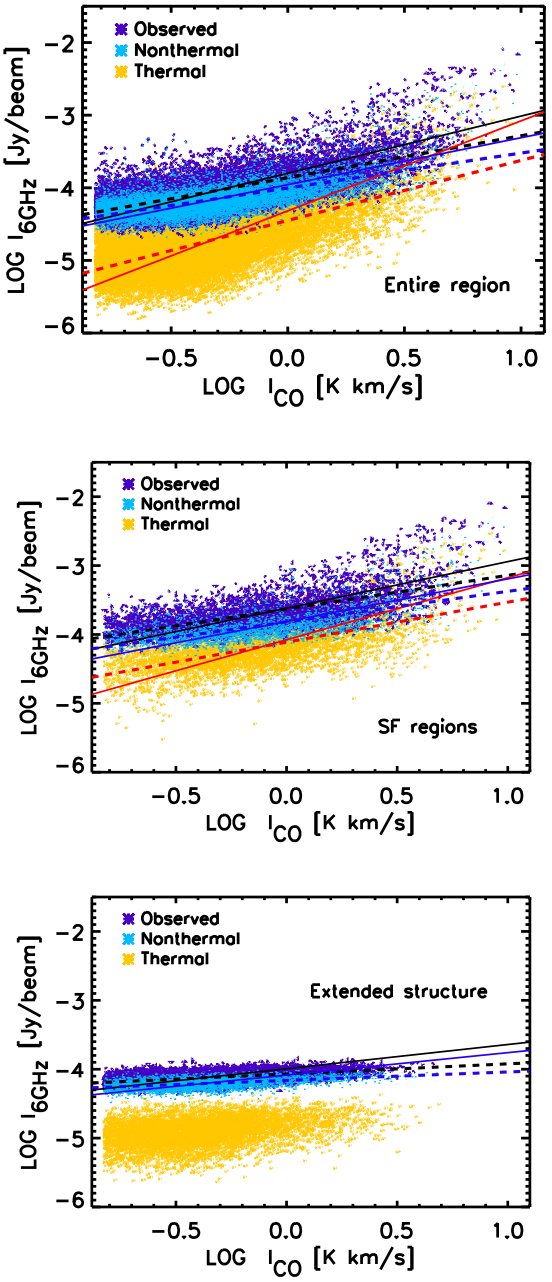

Figure 10. The 6.3 GHz RC correlation with the molecular gas traced by CO(2-1) line emission for the observed, NTH, and TH RC emission of the entire inner 18 × 18 arcmin^2 disc of M 33. Lines show the OLS bisector (solid) and OLS (dashed) fits for the observed (black), NTH (blue), and TH (red) RC–CO correlations.

Section 5.3). Investigating the structure of the magnetic field traced in polarization helps understanding its amplification mechanisms. This will be further addressed in a forthcoming paper.

Berkhuijsen, Beck & Tabatabaei (2013) showed that the correlation between the NTH RC and dust emission flattens due to diffusion of CRes. This can explain the relatively flat NTH RC–CO correlation obtained in the extended/diffuse RC emitting regions ($b^{\rm extended} = 0.29$ compared to $b^{\rm SF} = 0.67$, Table 9) as there the population of CRes is dominated by those that are diffused away from star-forming regions.

The resolved RC–CO correlation in more massive spiral galaxies, such as M51, is found to be tighter than in M 33 (Paladino et al. 2006; Schinnerer et al. 2013). This can be linked to a different molecular gas fraction and/or different physical conditions of the gas in these galaxies (e.g. mid-plane pressure; Mac Low & Glover 2012). The ISM is dominated by the atomic H I gas in M 33, unlike in M51 (Scoville & Young 1983). As shown by Druard et al. (2014), the molecular H_2 forms quiescently from the denser atomic clouds in M 33. Investigating the correlation between the RC and the HI-21 cm line emission in M 33, we find a large scatter ($r < 0.33$) and the correlations with the total neutral gas (H I + H_2) are weaker than those with the molecular gas. This is expected if most of the RC emission emerges from the star-forming regions in the molecular phase rather than in the atomic phase.

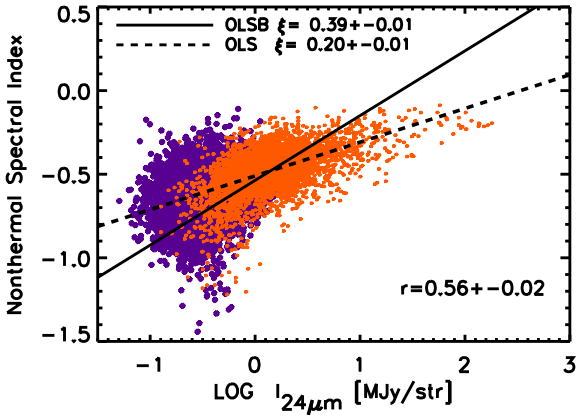

Figure 11. The NTH spectral index (obtained above a 2.5σ cut-off) becomes flatter with $\Sigma_{\rm SFR}$ traced by the 24 μm emission in star-forming regions (orange). Lines show the OLS bisector (OLSB, solid) and OLS (dashed) regressions. The Pearson correlation coefficient r is also indicated. No significant correlation holds in the extended/diffuse regions (violet points).

5.3 Impact of star formation on CRes and magnetic field

Massive star formation activity can change the physical state of the surrounding ISM by heating, ionization, and powerful winds. It can also inject turbulence, as well as high-energy particles and CRes with a flat spectrum. The latter can be investigated by mapping the pure synchrotron spectral index $\alpha_{\rm n}$ in galaxies. This map obtained for M 33 (Section 4.3) already indicates that the CRe energy spectrum is flatter in M 33's giant H II regions (Fig. 6). We further investigate if there is an overall trend between $\alpha_{\rm n}$ and $\Sigma_{\rm SFR}$ in this galaxy. For this purpose, we use a different SFR tracer, the 24 μm emission.[11] A correlation is found between $\alpha_{\rm n}$ and the 24 μm intensity, $I_{24\,\mu{\rm m}}$, with a Pearson coefficient of $r = 0.57 \pm 0.02$ (Fig. 11). For star-forming regions, i.e. after subtracting the diffuse emission, we find the following relation for 15 arcsec pixels[12]

$$\alpha_{\rm n} = \eta + \zeta \,.\, \log\left(\frac{I_{24\mu{\rm m}}}{\rm MJy\ sr^{-1}}\right), \qquad (10)$$

with $\eta = -0.536 \pm 0.003$ and $\zeta = 0.39 \pm 0.01$ using the bisector regression. We note that a flatter variation is found, $\zeta = 0.21 \pm 0.01$, using the OLS fitting. This shows that the flattening of the synchrotron spectrum with star formation is a general trend in the inner disc of M 33. The slope of variation ζ agrees with our

[11]The use of RC or Hα emission as SFR tracer may inject artificial correlations for this specific comparison.
[12]$\alpha_{\rm n}$ is recalculated using intensity maps with 15 arcsec pixels.

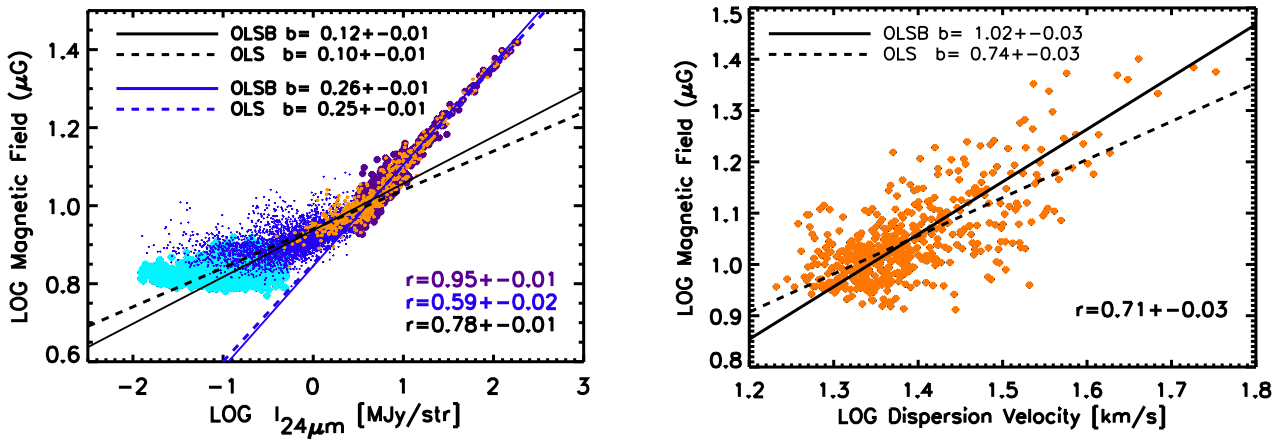

Figure 12. Left: the magnetic field strength versus $\Sigma_{\rm SFR}$ traced by the 24 μm emission. A bi-modal behaviour is found at $I_{24\,\mu m} \geq 3\,{\rm MJysr^{-1}}$ (magenta points) and below (blue points), i.e. depending on the SFR regime. Lines show the fits to the entire data (black) and the high-SFR regime (blue). No significant correlation is found in the extended/diffuse region (cyan points). Right: the magnetic field strength increases with the gas turbulent velocity (of H α lines) in a sample of bright star-forming regions. These regions are shown in the left-hand panel (orange points) as well. Lines show the OLS bisector (OLSB) and OLS regressions. The Pearson correlation coefficients r are also indicated.

global finding in the Key Insight in Nearby Galaxies Emitting in Radio (Tabatabaei et al. 2017) sample of galaxies: galaxies with higher $\Sigma_{\rm SFR}$ have a flatter synchrotron spectrum. This flattening was linked to the pitch-angle scattering of high-energy CRes in turbulent magnetic fields that is likely stronger in galaxies with higher SFRs. This might also explain the observed trend in M 33, as the magnetic field strength B increases with $\Sigma_{\rm SFR}$. Fig. 12 (left-hand panel) shows B versus $\Sigma_{\rm SFR}$ as traced by the 24 μm intensity, plotted using a 5σ rms cut. A best-fitting OLS bisector regression in the log-log plane results in the following relation

$$\log\left(\frac{\rm B}{\mu\rm G}\right) = a + b \times \log\left(\frac{\rm I_{24\,\mu m}}{\rm MJy\,sr^{-1}}\right), \quad (11)$$

with $a = 0.94 \pm 0.01$ and $b = 0.12 \pm 0.01$ and a Pearson correlation of $r = 0.76 \pm 0.01$ [black lines in Fig. 12(left)]. However, a steeper variation is inferred at SFRs higher than a certain level. In other words, the power-law proportionality of $\rm B \propto \Sigma_{SFR}^{\it b}$has a bi-model variation with

$$b = 0.26 \pm 0.01, \qquad I_{24\,\mu m} \geq 3\,{\rm MJy\,sr^{-1}},$$
$$b = 0.10 \pm 0.01, \qquad I_{24\,\mu m} < 3\,{\rm MJy\,sr^{-1}},$$

where the fits use the OLS bisector regression (indicated as OLSB in Fig. 12). The power-law index of $\simeq$0.26 obtained is close to the theoretical value of 0.3 proposed for the amplification of the magnetic field by a small-scale dynamo in SF regions (Schleicher & Beck 2013). This mechanism seems, however, not to be efficient in amplifying B at low SFRs as indicated by the flatter power-law index of $\simeq$0.10. If the magnetic field in SF regions is mainly amplified by the action of turbulence, a positive correlation is expected between B and gas turbulent velocity. We further investigate this by using the H α velocity dispersion measured for bright star-forming regions of M 33. The right-hand panel in Fig. 12 indeed shows a positive and linear correlation (OLSB fit) between the magnetic field strength and the turbulent velocity. Hence, star formation feedback increases the turbulent velocity of its surrounding gas. This turbulent energy is converted into magnetic energy, e.g. due to the dynamo action. This results in a turbulent and tangled magnetic field enhancement in the ISM.

As already mentioned in Section 1, previous studies show a relatively flat NTH spectrum in complexes of star-forming regions where the magnetic field is strong (Tabatabaei et al. 2007c, 2013a; Hassani et al. 2022), in agreement with our findings. This may seem counter-intuitive because synchrotron loss should increase with increasing magnetic field strength, assuming that the field is uniform. However, our studies show that the magnetic field is strongly tangled and non-uniform in star-forming complexes and, hence, CRes can experience pitch angle scattering (e.g. Tautz et al. 2013). These energetic CRes tend to stream in related dense plasma at a speed larger than the local Alfvén speed (which drops with density ρ as $v_{\rm A} = B/\sqrt{4\pi\rho}$), causing streaming instabilities (e.g. Marcowith, van Marle & Plotnikov 2021). As a result, the synchrotron emission observed in star-forming complexes is due to CRes with a short residence time in regions of strong turbulent magnetic fields. This results in a relatively flat spectrum because CRes do not have enough time to cool down efficiently by the magnetic field. These energetic CRes can have an important consequence for the energy balance of the ISM in star-forming regions, causing strong winds and outflows as a result of a pressure gradient imposed by them. The existence of an NTH halo in M 33, indicated through a detailed study of the radio-IR correlation (Tabatabaei et al. 2013b), is consistent with such a feedback. Observations of edge-on galaxies also agree with the cosmic ray-driven winds related to star-forming regions in galactic discs (Heesen et al. 2018).

We note that a flat synchrotron spectrum can also be maintained through other processes in the star-forming regions. As shown in Fig. 6, a fraction of the flat-spectrum regions appears as shells around the SNRs and giant H II complexes (with $\alpha_{\rm n} > -0.5$). Such features can be produced if CRes have gained additional energy due to re-acceleration in related shock fronts. Taking into account the resolution (pixel scale of $\leq$20 pc) of this study, detecting these features is not far from expectation, particularly in large complexes of star-forming regions in M 33.

6 SUMMARY

We study the structure and origin of the RC emission from the ISM of M 33 down to linear scales of $\simeq$30 pc (9.″3) and 50 pc (15 arcsec) by combining VLA interferometric observations at C and L bands with single-dish observations from the *100-m Effelsberg telescope*. The RC emission emerges from three main structural

components: bright star-forming regions, extended structures, and a diffuse disc. Separating these components helps in calibrating the SFR and addressing the effect of diffuse emission when using the RC maps. We also disentangle the TH and NTH processes in the star-forming and diffuse parts of the gaseous ISM. This helps us investigate the impact of massive star formation on the magnetic field and CRes and further resolve the nature and origin of feedback in M 33. The most important results and conclusions are summarized as follows.

(i) Radio sources contribute about 36 per cent (46 per cent) of the total RC emission at 1.5 GHz (6.3 GHz) in the inner 18×18 arcmin^2 disc of M 33 at 15 arcsec (50 pc) resolution. About half of these sources are H II regions (contributing 57 per cent and 74 per cent in total source emission at 1.5 and 6.3 GHz, respectively) and the rest, SNRs and background radio sources.

(ii) The diffuse RC emission has two different structural components, an extended structure with a spiral pattern covering parts of the optical arms and almost filling the inter-arm regions, and constituting $\simeq 20$ per centof the total RC, and a diffuse disc (+ halo) component of $\simeq 40$ per centcontribution. Both these components are dominated by the NTH synchrotron emission, particularly at the lower frequency of 1.5 GHz.

(iii) Excluding the diffuse components, we find a linear correlation between non-radio SFR tracers and the observed RC emission, based on which radio SFR calibration relations are provided.

(iv) Both the mean NTH synchrotron spectral index obtained between 1.5 and 6.3 GHz ($\alpha_n \simeq -0.7$, $I_{nt} \propto \nu^{\alpha_n}$) and the mean equipartition magnetic field strength ($B \simeq 7\,\mu$G) agree with those obtained by Tabatabaei et al. (2007b, 2008) based on previous *VLA* observations. The *VLA* observations uncover variations in α_n and B on spatial scales about 10 times smaller than observed before. We find that α_n becomes flatter with Σ_{SFR}, indicating the escape and re-acceleration of CRes. The magnetic field strength also increases with Σ_{SFR}, following a bimodal relation, i.e. changing the slope above a SFR threshold.

(v) Comparing the observed RC with the molecular gas emission, we find a tighter correlation in star-forming regions than in other regions. No significant correlation is found between the molecular gas and TH RC in the more quiescent and lower-density regions of the ISM. The NTH emission is, however, still correlated with the molecular gas in these regions. The TH RC–CO correlation in star-forming regions is in favour of a linear KS star formation law. This is in contrast with previous studies in M 33 where diffuse emission was included.

Similar studies in large samples of galaxies will shed light on the interplay between massive star formation and the ISM and its role in the evolution of SFR. The upcoming sensitive surveys with the Square Kilometer Array and the ngVLA will enable mapping the RC emission from diffuse ISM not only in nearby galaxies but also at higher redshifts.

ACKNOWLEDGEMENTS

JHK acknowledges financial support from the State Research Agency (AEI-MCINN) of the Spanish Ministry of Science and Innovation under the grant 'The structure and evolution of galaxies and their central regions' with reference PID2019-105602GB-I00/10.13039/501100011033, from the ACIISI, Consejería de Economía, Conocimiento y Empleo del Gobierno de Canarias and the European Regional Development Fund (ERDF) under grant with reference PROID2021010044, and from IAC project P/300724, financed by the Ministry of Science and Innovation, through the State Budget and by the Canary Islands Department of Economy, Knowledge and Employment, through the Regional Budget of the Autonomous Community. This research is partly based on observations made with the WHT operated on the island of La Palma by the Isaac Newton Group of Telescopes, in the Spanish Observatorio del Roque de Los Muchachos of the Instituto de Astrofísica de Canarias.

DATA AVAILABILITY

The data underlying this article are partly available in its supplementary material. The *VLA* raw data are available on *VLA* archive under the project ID, 11B-145. The reduced/calibrated *VLA* data corrected for missing short spacing is made available on figshare (10.6084/m9.figshare.21153112).

REFERENCES

Altenhoff W., Mezger P. G., Wendker H., Westerhout G., 1960, Veroff Sternwarte Bonn, 59, 48
Aniano G., Draine B. T., Gordon K. D., Sandstrom K., 2011, PASP, 123, 1218
Beck R., 1979, Ph.D. Thesis, Rheinische Friedrich-Wilhelms-Universitaet
Beck R., 2015, A&AR, 24, 4
Beck R., Krause M., 2005, Astron. Nachr., 326, 414
Berkhuijsen E. M., Beck R., Tabatabaei F. S., 2013, MNRAS, 435, 1598
Bigiel F., Leroy A., Walter F., Brinks E., de Blok W. J. G., Madore B., Thornley M. D., 2008, AJ, 136, 2846
Boquien M. et al., 2011, AJ, 142, 111
Boquien M. et al., 2015, A&A, 578, A8
Brunthaler A., Reid M. J., Falcke H., Greenhill L. J., Henkel C., 2005, Science, 307, 1440
Buczilowski U. R., Beck R., 1987, A&AS, 68, 171
Calzetti D., Armus L., Bohlin R. C., Kinney A. L., Koornneef J., Storchi-Bergmann T., 2000, ApJ, 533, 682
Chyży K. T., Weżgowiec M., Beck R., Bomans D. J., 2011, A&A, 529, A94
Condon J. J., 1992, ARA&A, 30, 575
Condon J. J., Cotton W. D., Greisen E. W., Yin Q. F., Perley R. A., Taylor G. B., Broderick J. J., 1998, AJ, 115, 1693
Corbelli E., Braine J., Tabatabaei F. S., 2020, A&A, 639, A27
Cotton W. D., 2008, PASP, 120, 439
Cotton W. D. et al., 2018, ApJ, 856, 67
Daigle O., Carignan C., Hernandez O., Chemin L., Amram P., 2006, MNRAS, 368, 1016
de Vaucouleurs G., Leach R. W., 1981, PASP, 93, 190
Deul E. R., van der Hulst J. M., 1987, A&AS, 67, 509
Dickinson C., Davies R. D., Davis R. J., 2003, MNRAS, 341, 369
Dodorico S., Sabbadin F., 1976, A&A, 53, 443
Druard C. et al., 2014, A&A, 567, A118
Dumas G., Schinnerer E., Tabatabaei F. S., Beck R., Velusamy T., Murphy E., 2011, AJ, 141, 41
Duric N., Viallefond F., Goss W. M., van der Hulst J. M., 1993, A&AS, 99, 217
Ferguson A. M. N., Wyse R. F. G., Gallagher J. S., Hunter D. A., 1998, ApJ, 506, L19
Fletcher A., 2001, Ph.D. Thesis. University of Newcastle
For B. Q. et al., 2018, MNRAS, 480, 2743
Freedman W. L., Wilson C. D., Madore B. F., 1991, ApJ, 372, 455
Gordon S. M., Duric N., Kirshner R. P., Goss W. M., Viallefond F., 1999, ApJS, 120, 247
Gordon K. D. et al., 2005, PASP, 117, 503
Gratier P. et al., 2010, A&A, 522, A3
Greenawalt B., Walterbos R. A. M., Thilker D., Hoopes C. G., 1998, ApJ, 506, 135
Gürkan G. et al., 2018, MNRAS, 475, 3010

Hassani H., Tabatabaei F., Hughes A., Chastenet J., McLeod A. F., Schinnerer E., Nasiri S., 2022, MNRAS, 510, 11
Heesen V., Brinks E., Leroy A. K., Heald G., Braun R., Bigiel F., Beck R., 2014, AJ, 147, 103
Heesen V. et al., 2018, MNRAS, 476, 158
Heyer M. H., Corbelli E., Schneider S. E., Young J. S., 2004, ApJ, 602, 723
Hoernes P., Berkhuijsen E. M., Xu C., 1998, A&A, 334, 57
Hoopes C. G., Walterbos R. A. M., 2000, ApJ, 541, 597
Isobe T., Feigelson E. D., Akritas M. G., Babu G. J., 1990, ApJ, 364, 104
Israel F. P., van der Kruit P. C., 1974, A&A, 32, 363
Kam Z. S., Carignan C., Chemin L., Amram P., Epinat B., 2015, MNRAS, 449, 4048
Kellermann K. I., Owen F. N., 1988, in Verschuur G. L., ed., Galactic and Extragalactic Radio Astronomy, 2nd edn. Springer-Verlag, Berlin, New York, p. 563
Kennicutt R. C., Jr, 1998, ARA&A, 36, 189
Kennicutt R. C., Jr et al., 2003, PASP, 115, 928
Kennicutt R. C., Jr, Lee J. C., Funes José G. S. J., Sakai S., Akiyama S., 2008, ApJS, 178, 247
Kouroumpatzakis K., Zezas A., Maragkoudakis A., Willner S. P., Bonfini P., Ashby M. L. N., Sell P. H., Jarrett T. H., 2021, MNRAS, 506, 3079
Kramer C. et al., 2010, A&A, 518, L67
Krause M. et al., 2018, A&A, 611, A72
Kreckel K. et al., 2013, ApJ, 771, 62
Kroupa P., 2001, MNRAS, 322, 231
Krügel E., 2003, IoP Series in Astronomy and Astrophysics. The Institute of Physics, Bristol, UK
Levenson N. A., Kirshner R. P., Blair W. P., Winkler P. F., 1995, AJ, 110, 739
Long K. S. et al., 2010, ApJS, 187, 495
Mac Low M.-M., Glover S. C. O., 2012, ApJ, 746, 135
Marcowith A., van Marle A. J., Plotnikov I., 2021, Phys. Plasmas, 28, 080601
Murgia M., Helfer T. T., Ekers R., Blitz L., Moscadelli L., Wong T., Paladino R., 2005, A&A, 437, 389
Murphy E. J. et al., 2011, ApJ, 737, 67
Niklas S., 1997, A&A, 322, 29
Paladino R., Murgia M., Helfer T. T., Wong T., Ekers R., Blitz L., Gregorini L., Moscadelli L., 2006, A&A, 456, 847
Perley R. A., Butler B. J., 2013, ApJS, 206, 16
Poglitsch A. et al., 2010, A&A, 518, L2
Price R., Duric N., 1992, ApJ, 401, 81
Regan M. W., Vogel S. N., 1994, ApJ, 434, 536
Rieke G. H. et al., 2004, ApJS, 154, 25
Roussel H., 2013, PASP, 125, 1126
Schinnerer E. et al., 2013, ApJ, 779, 42
Schleicher D. R. G., Beck R., 2013, A&A, 556, A142
Scoville N., Young J. S., 1983, ApJ, 265, 148
Smith D. J. B. et al., 2021, A&A, 648, A6
Tabatabaei F. S. et al., 2007a, A&A, 466, 509
Tabatabaei F. S., Krause M., Beck R., 2007b, A&A, 472, 785
Tabatabaei F. S., Beck R., Krügel E., Krause M., Berkhuijsen E. M., Gordon K. D., Menten K. M., 2007c, A&A, 475, 133
Tabatabaei F. S., Krause M., Fletcher A., Beck R., 2008, A&A, 490, 1005
Tabatabaei F. S. et al., 2013a, A&A, 552, A19
Tabatabaei F. S., Berkhuijsen E. M., Frick P., Beck R., Schinnerer E., 2013b, A&A, 557, 129
Tabatabaei F. S. et al., 2014, A&A, 561, A95
Tabatabaei F. S. et al., 2017, ApJ, 836, 185
Tabatabaei F. S., Minguez P., Prieto M. A., Fernández-Ontiveros J. A., 2018, Nature Astron., 2, 83
Tacchella S. et al., 2022, MNRAS, 513, 2904
Tautz R. C., Dosch A., Effenberger F., Fichtner H., Kopp A., 2013, A&A, 558, A147
Tüllmann R. et al., 2009, ApJ, 707, 1361
Verley S. et al., 2010, A&A, 518, L68
Viallefond F., Goss W. M., van der Hulst J. M., Crane P. C., 1986, A&AS, 64, 237
Völk H. J., 1989, A&A, 218, 67
von Kap-Herr A., Berkhuijsen E. M., Wielebinski R., 1978, A&A, 62, 51
Wang Y., Gao J., Ren Y., Chen B., 2022, ApJS, 260, 41
Weingartner J. C., Draine B. T., 2001, ApJ, 548, 296
White R. L., Long K. S., Becker R. H., Blair W. P., Helfand D. J., Winkler P. F., 2019, ApJS, 241, 37
Williams T. G., Gear W. K., Smith M. W. L., 2018, MNRAS, 479, 297

SUPPORTING INFORMATION

Supplementary data are available at *MNRAS* online.

Table_5_supplementary.pdf
Table_6_supplementary.pdf

Please note: Oxford University Press is not responsible for the content or functionality of any supporting materials supplied by the authors. Any queries (other than missing material) should be directed to the corresponding author for the article.

This paper has been typeset from a TEX/LATEX file prepared by the author.